# Development of a finite volume model for the compressible gap flow inside a screw pump

Dipl.-Ing. (FH) Klaus Räbiger
Prof. Dr. T.M.A. Maksoud
Prof. Dr. John Ward

University of Glamorgan
School of Technology
Wales, UK

Prof. Dr. G. Hausmann

Georg-Simon-Ohm Fachhochschule Nürnberg
Fachbereich Maschinenbau und
Versorgungstechnik

Abstract

Screw pumps are widely used in conditions of operation, where a constant flow rate and low pulsation are desirable. The type of screw pump, whose gaps are theoretically investigated in this paper, is a twin screw pump, which is used for multiphase operations. Due to the lack of knowledge concerning the pumping behaviour at very high gas volume fractions up to 100 %, the compressible gap flow inside a screw pump has to be investigated with techniques such as computational fluid dynamics more accurately. The development of a finite volume model for the compressible flow in each gap allows a prediction of the thermodynamic behaviour and of the inner leakage flow rate and thus, the effective flow rate of the pump. The resulting pressure and temperature distributions will enhance the understanding of the pump operation.

Key words : screw pump - finite volume - gas volume fraction

ISSN 1616-0762 Sonderdruck Schriftenreihe der Georg-Simon-Ohm-Fachhochschule Nürnberg Nr. 30, Juli 2005

# 1. Introduction and literature survey

A screw pump is a special type of rotary displacement pumps, in which a number of screws rotates inside a cylindrical housing. The geometry and rotation of the screws generate a series of closed chambers, which transport the fluid from the low pressure inlet to the high pressure outlet, see figure 1.1.

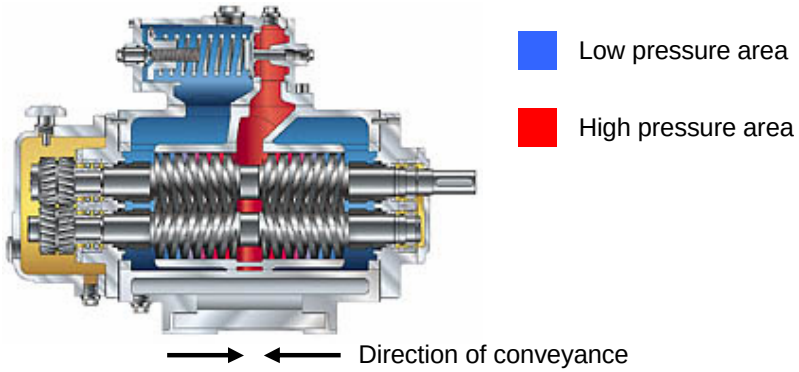


Figure 1.1 : Multiphase screw pump

The pressure distribution through the pump and hence the flow characteristics and system performance is heavily influenced by leakage of the fluid from the discharge side back to the suction side. This leakage flow occurs through three different gaps inside the screw pump, namely the perimeter gap between the screws and the housing, and the radial and flank gaps between the mating surfaces of the screws, see figure 1.2.

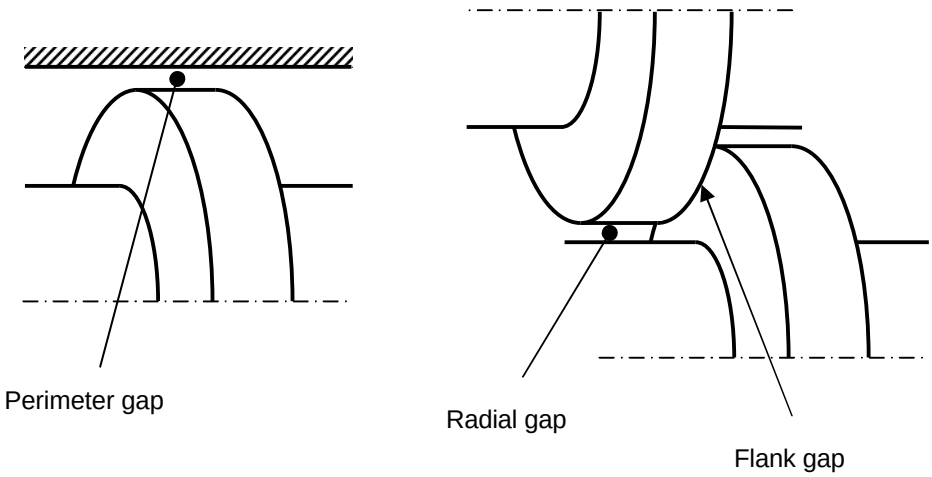


Figure 1.2 : Three different kind of gaps inside the screw pump

Previous investigations of multiphase screw pumps have largely been concerned with the general pumping behaviour of these systems, [1]. Moreover these studies have been restricted to relatively medium sized pumps, in which the maximum power consumption and gas concentrations are relatively modest. In these situations the heat capacity and density of the gas-liquid mixture is dominated by the liquid phase so that the pumping process is mainly isothermal and thermodynamic effects can be neglected, [2] and [3]. However, this assumption cannot be justified for larger, more powerful screw pumps, which are capable of conveying two-phase fluids with very high concentrations of the gaseous phase up to 100 %. On the other hand, past investigations used a more simple theory for the flow through the gaps and often neglect the compressibility of the gaseous phase. Another area of research is the application of screw pumps in blood conveyance. With the focus on low hemolysis, a channel flow model was introduced to investigate the velocity field, the flow rate and the shear stress distribution, [4]. The model was solved by a finite analytical method, with the assumptions, that the fluid is incompressible and the flow is fully developed in channel direction.

Due to the above-mentioned lack of accurate models, it was necessary to create models for the gap flow, using computational fluid dynamic, to predict the leakage flow more accurately. Because of validation reasons and the fact that this first modelling stage refers only to single-phase fluids, the CFD model for the compressible gap flow was analysed for air as an ideal gas.

## 2. Conservation equations for the gap flow

The governing equations for the flow field inside the three identified gaps can be represented by the compressible Navier-Stokes equation in a vector form as

$$\frac{\partial}{\partial t}\boldsymbol{I}+\frac{\partial}{\partial x}\boldsymbol{J}+\frac{\partial}{\partial y}\boldsymbol{K}+\frac{\partial}{\partial z}\boldsymbol{L}=\boldsymbol{0} \tag{2.1}$$

The components of each vector represent sequentially the conservation equations of mass, momentum in three space directions, and finally energy.

Vector, which represents the unsteady term of equation 2.1

$$\boldsymbol{I}=\begin{bmatrix} \rho \\ \rho\cdot u \\ \rho\cdot v \\ \rho\cdot w \\ \rho\cdot\left(\dfrac{p\cdot c_V}{\rho\cdot R}+\dfrac{\left(u^2+v^2+w^2\right)}{2}\right) \end{bmatrix} \tag{2.2}$$

Vector, which represents the steady component of equation 2.1 in the x - coordinate direction

$$\boldsymbol{J}=\begin{bmatrix} \rho\cdot u \\ \rho\cdot u\cdot u+p-\tau_{xx} \\ \rho\cdot u\cdot v-\tau_{xy} \\ \rho\cdot w\cdot u-\tau_{xz} \\ \rho\cdot u\cdot\left(\dfrac{p\cdot c_V}{\rho\cdot R}+\dfrac{\left(u^2+v^2+w^2\right)}{2}\right)+u\cdot p-u\cdot\tau_{xx}-v\cdot\tau_{xy}-w\cdot\tau_{xz}-k\cdot\dfrac{\partial T}{\partial x} \end{bmatrix} \tag{2.3}$$

Vector, which represents the steady component of equation 2.1 in the y - coordinate direction

$$\boldsymbol{K}=\begin{bmatrix} \rho\cdot v \\ \rho\cdot u\cdot v-\tau_{xy} \\ \rho\cdot v\cdot v+p-\tau_{yy} \\ \rho\cdot w\cdot v-\tau_{zy} \\ \rho\cdot v\cdot\left(\dfrac{p\cdot c_V}{\rho\cdot R}+\dfrac{\left(u^2+v^2+w^2\right)}{2}\right)+v\cdot p-u\cdot\tau_{yx}-v\cdot\tau_{yy}-w\cdot\tau_{yz}-k\cdot\dfrac{\partial T}{\partial y} \end{bmatrix} \tag{2.4}$$

Vector, which represents the steady component of equation 2.1 in the z - coordinate direction

$$\boldsymbol{L} = \begin{bmatrix} \rho \cdot w \\ \rho \cdot u \cdot w - \tau_{xz} \\ \rho \cdot v \cdot w - \tau_{yz} \\ \rho \cdot w \cdot w + p - \tau_{zz} \\ \rho \cdot w \cdot \left( \dfrac{p \cdot c_V}{\rho \cdot R} + \dfrac{\left(u^2 + v^2 + w^2\right)}{2} \right) + w \cdot p - u \cdot \tau_{zx} - v \cdot \tau_{zy} - w \cdot \tau_{zz} - k \cdot \dfrac{\partial T}{\partial z} \end{bmatrix} \tag{2.5}$$

## 3. Finite volume approach

The finite volume method is similar to finite differences method (FDM) in that it is a very efficient calculation method in the field of computational fluid dynamics and is characterised as having a high accuracy compared to finite element method (FEM) and by a higher flexibility compared to the FDM.

The finite volume approach, [5] and [6], is to integrate the derivative terms in the Navier-Stokes equations with respect to the three space coordinates over the whole flow domain and then transform the results with the divergence theorem by Gauss.

Integration of the Navier-Stokes equation

$$\iiint_V \left( \frac{\partial}{\partial t} \boldsymbol{I} \right) dV + \iiint_V \left( \frac{\partial}{\partial x} \boldsymbol{J} \right) dV + \iiint_V \left( \frac{\partial}{\partial y} \boldsymbol{K} \right) dV + \iiint_V \left( \frac{\partial}{\partial z} \boldsymbol{L} \right) dV = 0 \tag{3.1}$$

Divergence theorem by Gauss

$$\iiint_V div\boldsymbol{F}\, dV = \iint_A \boldsymbol{F}\, d\boldsymbol{A} = \iint_A \left(\boldsymbol{F} \cdot \boldsymbol{n}\right) dA \tag{3.2}$$

$$\boldsymbol{A}_l = \boldsymbol{n}_l \cdot A_l \tag{3.3}$$

Resulting equation (formulation for each cell of the whole flow domain)

$$\frac{d}{dt} \boldsymbol{I}_{i,j,k} \cdot V_{i,j,k} + \sum_{m=1}^{3} \sum_{l=1}^{6} \left( \boldsymbol{F}_{ml} \cdot A_{ml} \right)_{ijk} = 0 \tag{3.4}$$

with m = 1 ... 3 for each derivative in the three coordinate directions
l = 1 ... 6 for each face of the cell, here with a cuboid's shape

The resulting equation 3.4 is already formulated for a 3-dimensional finite volume cell, which will be generated by a structured discretisation of the whole flow domain. As an example, a single cell with all notations can be seen below in figure 3.1.

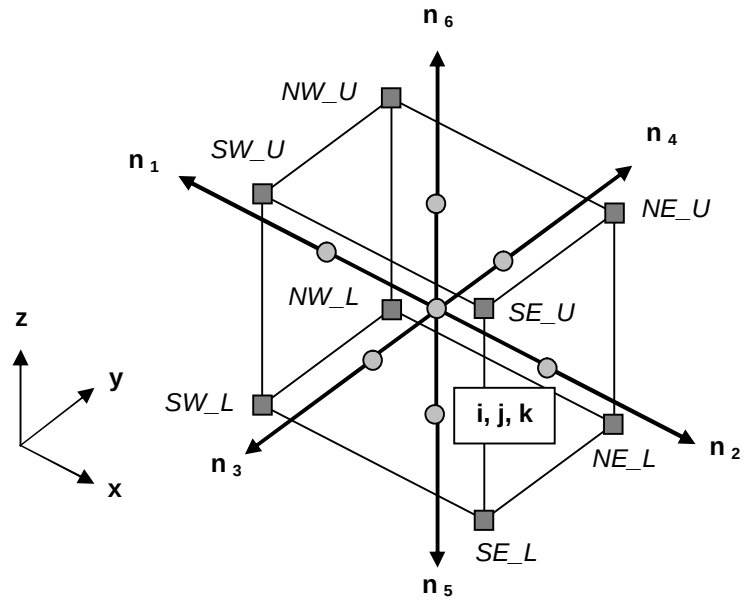


Figure 3.1 : 3-dimensional finite volume cell

The following form of equation 3.4 allows their direct use for the numerical calculation.

$$\frac{d}{dt}\boldsymbol{I}_{i,j,k} = -\frac{1}{V_{i,j,k}} \cdot \begin{bmatrix} (\boldsymbol{J}_1 \cdot A_{11}) + (\boldsymbol{J}_2 \cdot A_{12}) + (\boldsymbol{J}_3 \cdot A_{13}) + \\ (\boldsymbol{J}_4 \cdot A_{14}) + (\boldsymbol{J}_5 \cdot A_{15}) + (\boldsymbol{J}_6 \cdot A_{16}) + \\ (\boldsymbol{K}_1 \cdot A_{21}) + (\boldsymbol{K}_2 \cdot A_{22}) + (\boldsymbol{K}_3 \cdot A_{23}) + \\ (\boldsymbol{K}_4 \cdot A_{24}) + (\boldsymbol{K}_5 \cdot A_{25}) + (\boldsymbol{K}_6 \cdot A_{26}) + \\ (\boldsymbol{L}_1 \cdot A_{31}) + (\boldsymbol{L}_2 \cdot A_{32}) + (\boldsymbol{L}_3 \cdot A_{33}) + \\ (\boldsymbol{L}_4 \cdot A_{34}) + (\boldsymbol{L}_5 \cdot A_{35}) + (\boldsymbol{L}_6 \cdot A_{36}) \end{bmatrix} \tag{3.5}$$

In the above expression 3.5, the vector ***I*** is defined by the flow condition in the centre of the cell (cell-centred formulation). The vectors ***J***, ***K*** and ***L*** are calculated against it in the middle of the six cell faces $A_1$ to $A_6$ by averaged state values of two neighbouring cells.

## 4. Flux-difference splitting scheme

The flux vector ***J*** (see equation 2.3) can be splitted - as well as the flux vectors ***K*** and ***L*** - into two vectors $\boldsymbol{J}_c$ and $\boldsymbol{J}_d$, which contain on the one side all the convective and on the other side all the diffusive parts.

$$\boldsymbol{J}_c = \begin{bmatrix} \rho \cdot u \\ \rho \cdot u \cdot u + p \\ \rho \cdot u \cdot v \\ \rho \cdot w \cdot u \\ \rho \cdot u \cdot \left( \frac{p \cdot c_V}{\rho \cdot R} + \frac{\left(u^2 + v^2 + w^2\right)}{2} \right) + u \cdot p \end{bmatrix} \tag{4.1}$$

$$\boldsymbol{J}_d = \begin{bmatrix} 0 \\ -\tau_{xx} \\ -\tau_{xy} \\ -\tau_{xz} \\ -u\cdot\tau_{xx} - v\cdot\tau_{xy} - w\cdot\tau_{xz} - k\cdot\dfrac{\partial T}{\partial x} \end{bmatrix} \tag{4.2}$$

In contrast to the diffusive fluxes at the cell faces, which can be determined by a central difference scheme, the convective fluxes have to be calculated in a special manner, which supplies, especially the Runge-Kutta scheme, with enough dissipation to prevent possibly arising instabilities. An often used algorithm to calculate the convective flux, is Roe's approximate Riemann solver, [7], which belongs to the flux-difference splitting schemes.

The convective flux through an arbitrary western cell face, see figure 4.1, follows to

$$\boldsymbol{J}_{c,W} = \tfrac{1}{2}\cdot\left[\boldsymbol{J}_c\left(\boldsymbol{I}_R\right) + \boldsymbol{J}_c\left(\boldsymbol{I}_L\right)\right] - \tfrac{1}{2}\cdot\left|\boldsymbol{A}_{Roe}\right|_W\cdot\left(\boldsymbol{I}_R - \boldsymbol{I}_L\right) \tag{4.3}$$

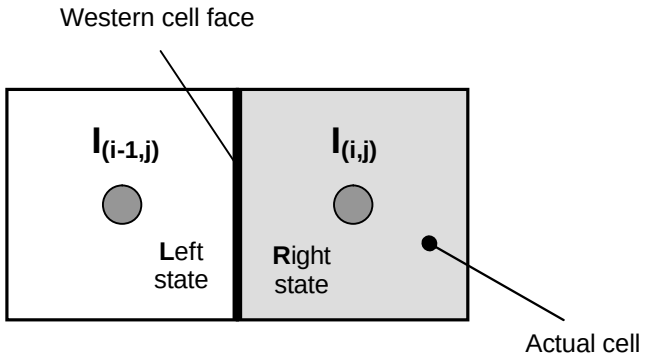


Figure 4.1 : Western cell face and their neighbouring cells

The expression 4.3 is similar to a normal central difference scheme, which includes a dissipation term. The Roe-Matrix $\boldsymbol{A}_{\text{Roe}}$ at the current cell face will correspond to the gradient of the convective flux vector with respect to the vector of the conservative variables, if the Roe-averaged variables are used.

The Roe-averaging is a special interpolation scheme of the cell-centre variables of the two neighbouring cells. For the conservative variables follows

$$\tilde{\rho} = \sqrt{\rho_L\cdot\rho_R} \tag{4.4}$$

$$\tilde{u} = \frac{u_L\cdot\sqrt{\rho_L} + u_R\cdot\sqrt{\rho_R}}{\sqrt{\rho_L} + \sqrt{\rho_R}} \tag{4.5}$$

$$\tilde{v} = \frac{v_L\cdot\sqrt{\rho_L} + v_R\cdot\sqrt{\rho_R}}{\sqrt{\rho_L} + \sqrt{\rho_R}} \tag{4.6}$$

$$\tilde{w} = \frac{w_L\cdot\sqrt{\rho_L} + w_R\cdot\sqrt{\rho_R}}{\sqrt{\rho_L} + \sqrt{\rho_R}} \tag{4.7}$$

$$\tilde{H} = \frac{H_L \cdot \sqrt{\rho_L} + H_R \cdot \sqrt{\rho_R}}{\sqrt{\rho_L} + \sqrt{\rho_R}} \tag{4.8}$$

with $$H = E + \frac{p}{\rho} = c_v \cdot T + \frac{\left(u^2 + v^2 + w^2\right)}{2} + \frac{p}{\rho} \tag{4.9}$$

## 5. Preconditioning

For compressible flows at low Mach numbers, the fluid is almost incompressible. In this case, the system of time-dependent, density-based Navier-Stokes equations will become very stiff. The rate of stiffness can be explained as the ratio of the largest to smallest eigenvalue. The eigenvalues of such a system are

| | | |
|---|---|---|
| $\boldsymbol{v} - a$ | with | **v** : total flow speed |
| $\boldsymbol{v}$ | | a : speed of sound |
| $\boldsymbol{v} + a$ | | |

The central idea of preconditioning, [8], is a creation of a premultiplication matrix for the unsteady terms in the Navier-Stokes equations, which changes the eigenvalues in such a manner, that they get closer together. Due to the fact, that the eigenvalues will have a similar magnitude, the transient vector will be transformed from conservative to primitive variables and premultiplied by the preconditioning matrix.

The transformation process includes the following steps:

The origin is equal to the vector ***I***, which contains all transient terms, represented by conservative variables - see term 2.2.

The Jacobian matrix of this vector with respect to the primitive variables

$$\frac{\partial \boldsymbol{I}}{\partial \boldsymbol{P}} = \begin{bmatrix} \rho_p & 0 & 0 & 0 & \rho_T \\ \rho_p \cdot u & \rho & 0 & 0 & \rho_T \cdot u \\ \rho_p \cdot v & 0 & \rho & 0 & \rho_T \cdot v \\ \rho_p \cdot w & 0 & 0 & \rho & \rho_T \cdot w \\ \rho_p \cdot H - 1 & \rho \cdot u & \rho \cdot v & \rho \cdot w & \rho_T \cdot H + \rho \cdot c_p \end{bmatrix} \tag{5.1}$$

with $$\rho_p = \left.\frac{\partial \rho}{\partial p}\right|_T \tag{5.2}$$ and $$\rho_T = \left.\frac{\partial \rho}{\partial T}\right|_p \tag{5.3}$$

and the vector with all unsteady terms, represented by primitive variables

$$\boldsymbol{P} = \begin{bmatrix} p \\ u \\ v \\ w \\ T \end{bmatrix} \tag{5.4}$$ , will be embedded in the following expression

$$\frac{\partial \boldsymbol{I}}{\partial \boldsymbol{P}} \cdot \frac{\partial}{\partial t} \iiint_V \boldsymbol{P}\, dV + \iiint_V \left( \frac{\partial}{\partial x} \boldsymbol{J} \right) dV + \iiint_V \left( \frac{\partial}{\partial y} \boldsymbol{K} \right) dV + \iiint_V \left( \frac{\partial}{\partial z} \boldsymbol{L} \right) dV = 0 \tag{5.5}$$

After some additional mathematical operations, for further details see references [7] and [8], the preconditioning matrix and it's implementation are:

$$\boldsymbol{Q} = \begin{bmatrix} \Theta & 0 & 0 & 0 & \rho_T \\ \Theta \cdot u & \rho & 0 & 0 & \rho_T \cdot u \\ \Theta \cdot v & 0 & \rho & 0 & \rho_T \cdot v \\ \Theta \cdot w & 0 & 0 & \rho & \rho_T \cdot w \\ \Theta \cdot H - 1 & \rho \cdot u & \rho \cdot v & \rho \cdot w & \rho_T \cdot H + \rho \cdot c_p \end{bmatrix} \tag{5.6}$$

$$\text{with} \qquad \Theta = \left( \frac{1}{v_{ref}^2} - \frac{\rho_T}{\rho \cdot c_p} \right) \tag{5.7}$$

$$\boldsymbol{Q} \cdot \frac{\partial}{\partial t} \iiint_V \boldsymbol{P}\, dV + \iiint_V \left( \frac{\partial}{\partial x} \boldsymbol{J} \right) dV + \iiint_V \left( \frac{\partial}{\partial y} \boldsymbol{K} \right) dV + \iiint_V \left( \frac{\partial}{\partial z} \boldsymbol{L} \right) dV = 0 \tag{5.8}$$

## 6. Time stepping method for the gap flow

The time stepping method, which was chosen for this implementation is a fourth-order Runge-Kutta scheme, [6], (fourth-order accuracy in time).

$$\boldsymbol{P}_{i,j,k}^{(0)} = \boldsymbol{P}_{i,j,k}^{(n)} \tag{6.1}$$

$$\boldsymbol{P}_{i,j,k}^{(1)} = \boldsymbol{P}_{i,j,k}^{(0)} - a_1 \cdot \frac{\Delta t}{V_{i,j,k}} \cdot \boldsymbol{R}^{(0)} \tag{6.2}$$

$$\boldsymbol{P}_{i,j,k}^{(2)} = \boldsymbol{P}_{i,j,k}^{(0)} - a_2 \cdot \frac{\Delta t}{V_{i,j,k}} \cdot \boldsymbol{R}^{(1)} \tag{6.3}$$

$$\boldsymbol{P}_{i,j,k}^{(3)} = \boldsymbol{P}_{i,j,k}^{(0)} - a_3 \cdot \frac{\Delta t}{V_{i,j,k}} \cdot \boldsymbol{R}^{(2)} \tag{6.4}$$

$$\boldsymbol{P}_{i,j,k}^{(4)} = \boldsymbol{P}_{i,j,k}^{(0)} - a_4 \cdot \frac{\Delta t}{V_{i,j,k}} \cdot \left( \frac{\boldsymbol{R}^{(0)} + 2 \cdot \boldsymbol{R}^{(1)} + 2 \cdot \boldsymbol{R}^{(2)} + \boldsymbol{R}^{(3)}}{6} \right) \tag{6.5}$$

$$\boldsymbol{P}_{i,j,k}^{(n+1)} = \boldsymbol{P}_{i,j,k}^{(4)} \tag{6.6}$$

with $a_1 = 1/2$ , $a_2 = 1/2$ , $a_3 = 1$ and $a_4 = 1$

The vector ***R*** of the RHS contains all the convective and diffusive fluxes and is expressed by the conservative variables. Because of the preconditioning, the transient vector ***P*** includes the primitive variables, so that a re-transformation of variables is necessary at the end of each cell calculation.

# 7. Discussion of results

## 7.1 The perimeter gap

The figures 7.1 and 7.2 show the distributions of the velocities in x- and y-direction as a function of the gap height and length inside the perimeter gap, which has a total height of 100 micrometers. In the case of a parabolic velocity profile in x-direction, the viscous force, which is defined by the gradient of the velocity component u in y-direction multiplied with the dynamic viscosity and the wetted area, must be equal to the sum of the pressure forces normal to the channel inlet and outlet.

The figures 7.3 to 7.5 represent the normal behaviour of a compressible gap flow. The density decreases as well as the pressure. The negative pressure gradient in flow direction is the driving force for the fluid motion. The difference between the inlet and the outlet pressure will lead to the above mentioned second force.

The temperature should normally also decreases, but the viscous forces which act on the fluid can heat up the flow through the gap. An indicator for this presumption can be seen in figure 7.5, where the region close to the wall (highest shear stresses) has higher temperature values in contrast to the middle of the gap, where the shear stress is becoming zero.

The figures 7.6 and 7.7 show the time history of the flow variables density, velocities in x- and y-direction, and pressure and also their residuals. All the time-dependent variables should reach a steady-state at the end. For a better verification also the residuals were determined. The residuals are the differences of the flow variables of two consecutive iteration steps and should become smaller with each time step. In the ideal case, they become zero.

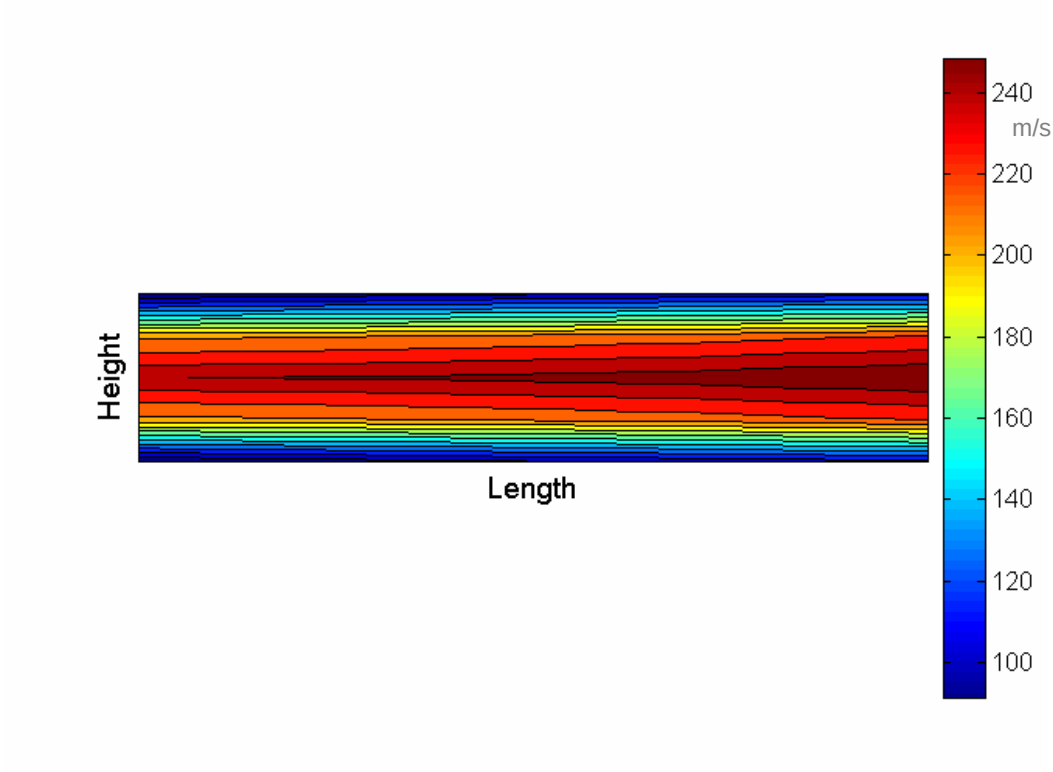


Figure 7.1 : Contour plot of the velocity component u

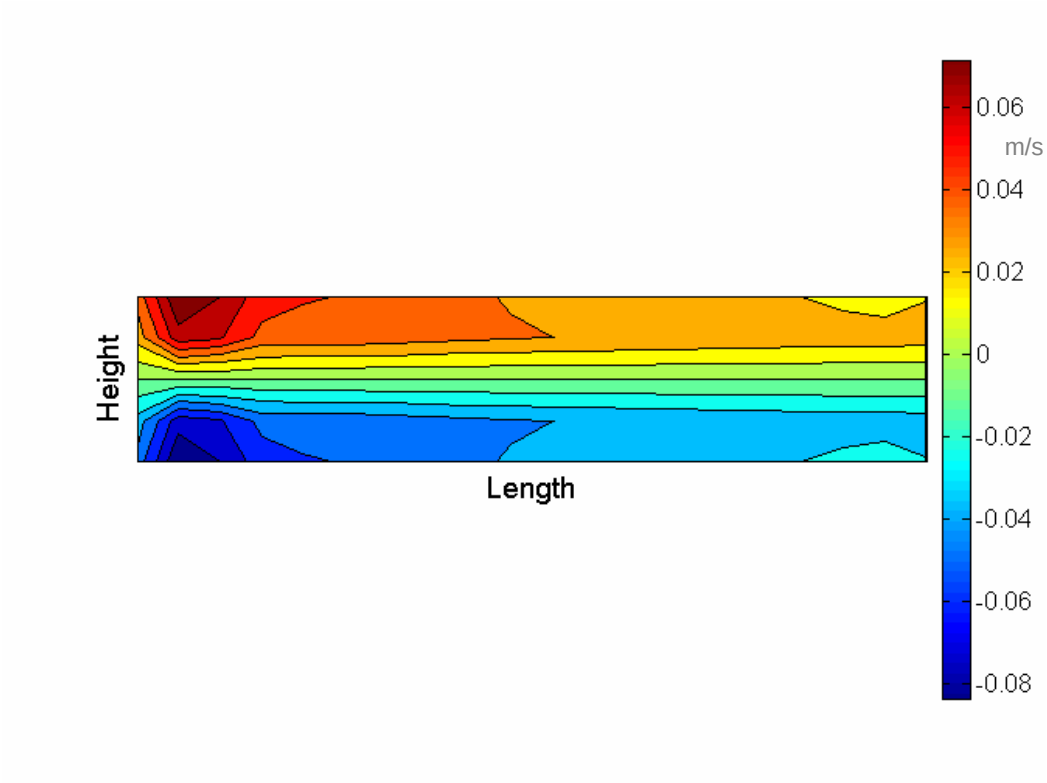


Figure 7.2 : Contour plot of the velocity component v

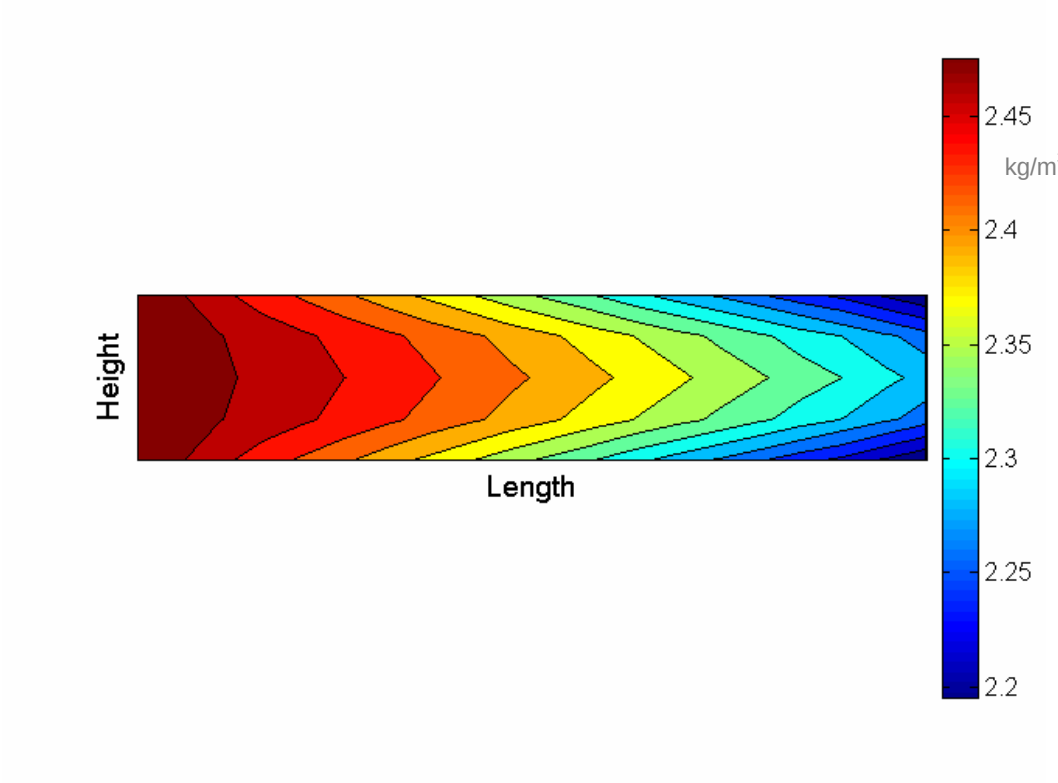


Figure 7.3 : Contour plot of the density

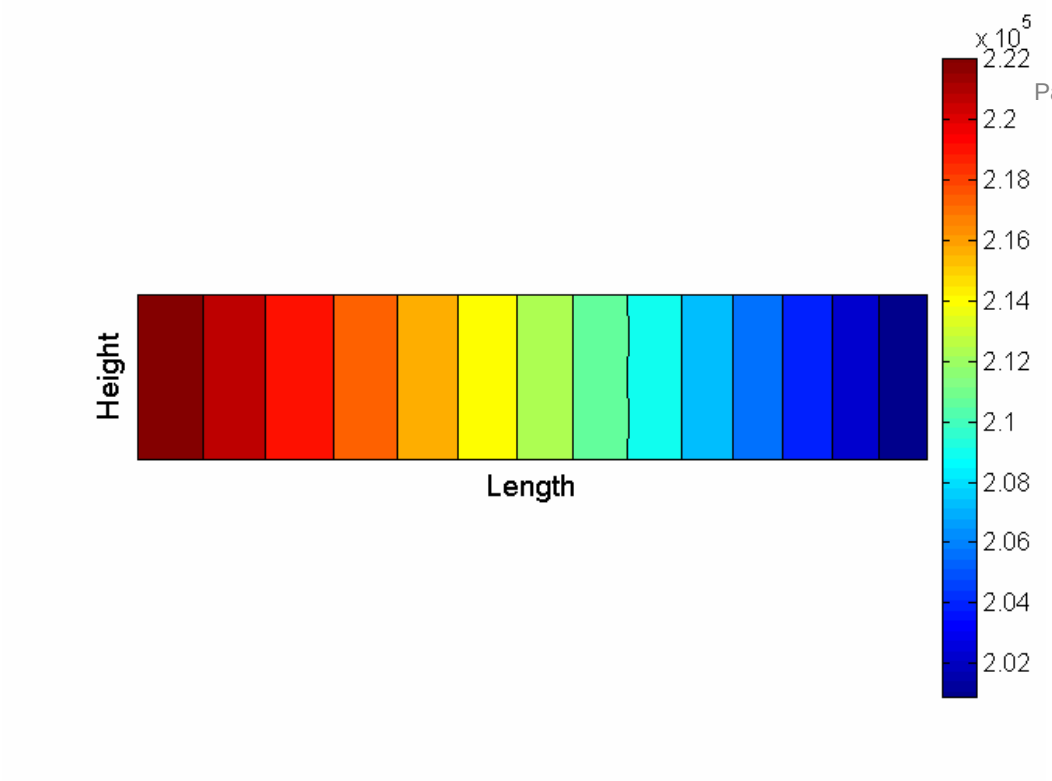


Figure 7.4 : Contour plot of the pressure

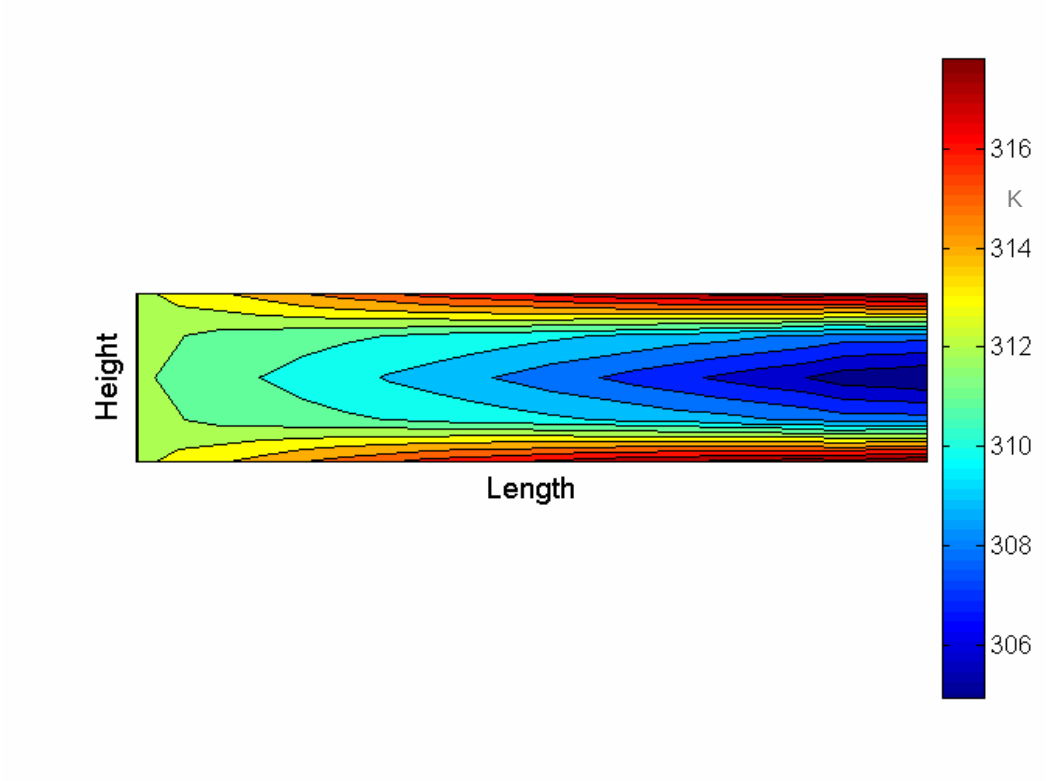


Figure 7.5 : Contour plot of the temperature

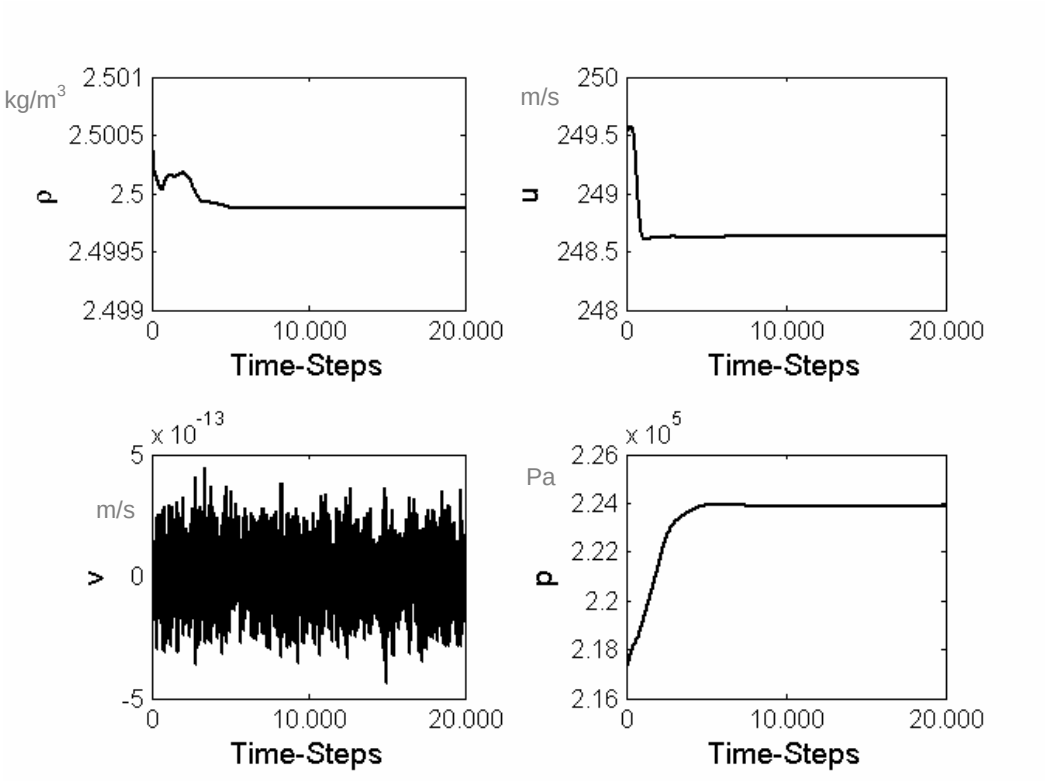


Figure 7.6 : Flow variables as a function of time-steps

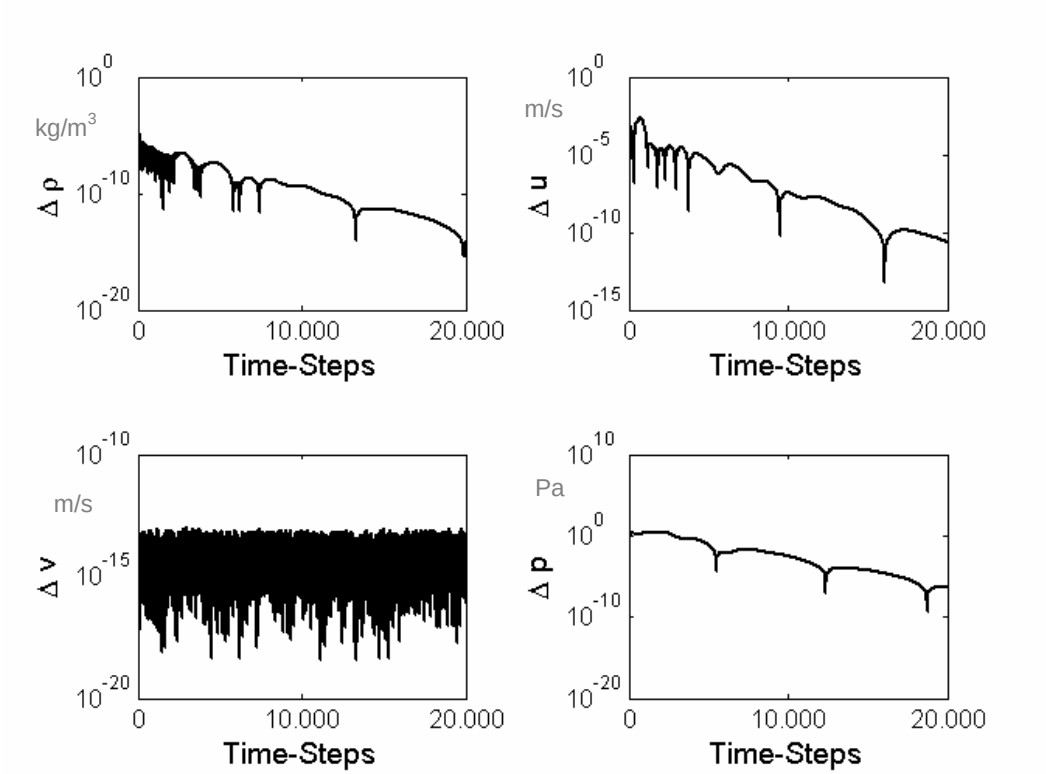


Figure 7.7 : Residuals (logarithmic) as a function of time-steps

## 7.2 The radial gap

The radial gap - see the white cells in figure 7.8 - is defined by two counter-rotating wheels and has a minimum height of 25 micrometers in this case. The driving forces in this gap, as well as in the general case of the perimeter gap, are the rotating or moving walls and the pressure gradient along the gap axis, where the pressure difference plays the major role.

Figure 7.9 shows the pressure distribution inside the radial gap. The reasons for this distribution are the firstly convergent gap shape and therefore the resulting fluid acceleration and the frictional pressure drop. Due to the large frictional pressure drop, the acceleration pressure drop below the outlet pressure can be seen only to a little extent in the last third of the radial gap.

The time history and the logarithmic residuals of the conservative flow variables as a function of time-steps can be seen finally in the figures 7.10 and 7.11.

Figure 7.8 : Gap geometry in the nip region with surrounding dummy cells

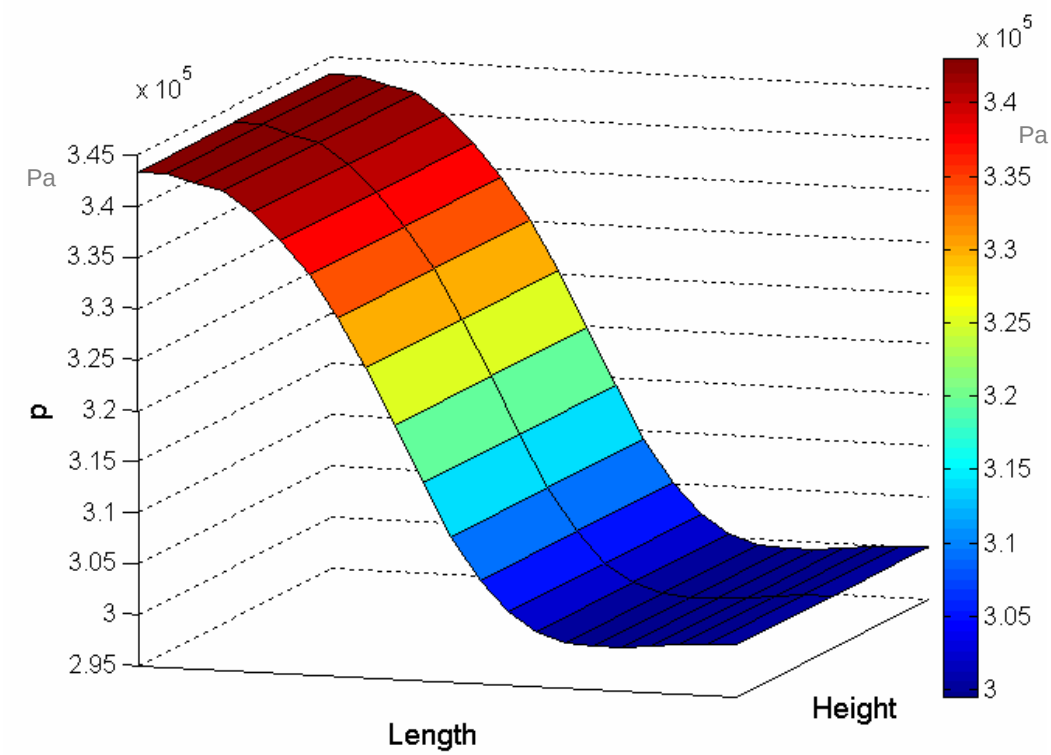


Figure 7.9 : Pressure distribution in the nip region

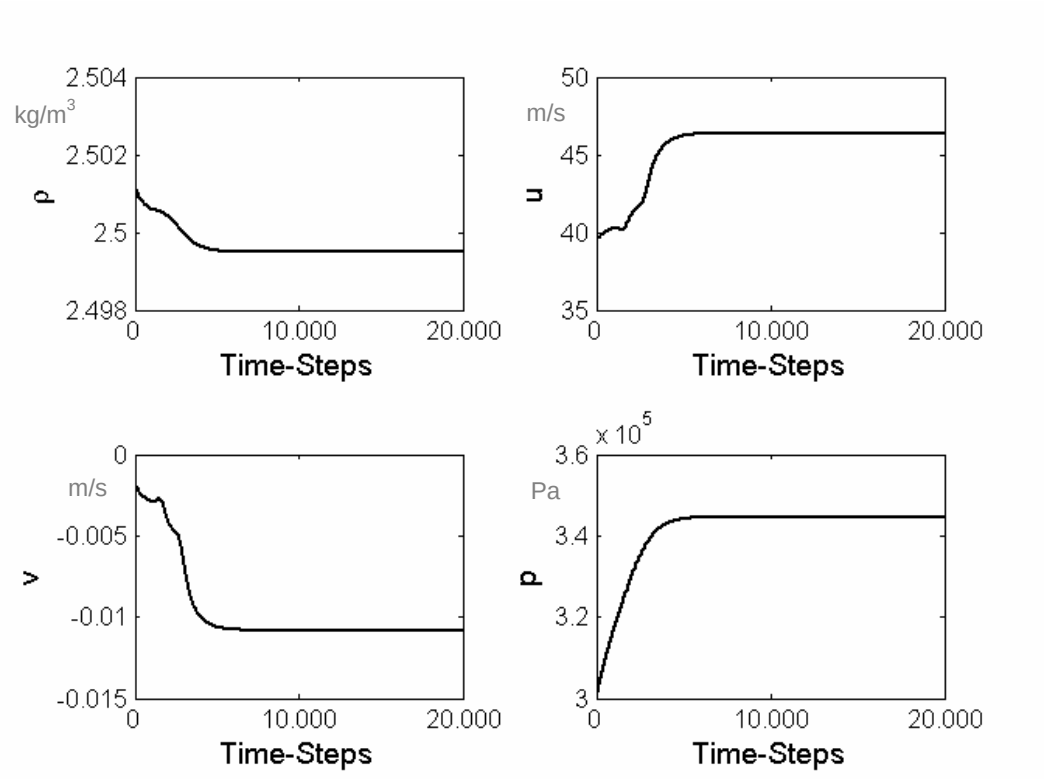


Figure 7.10 : Flow variables as a function of time-steps

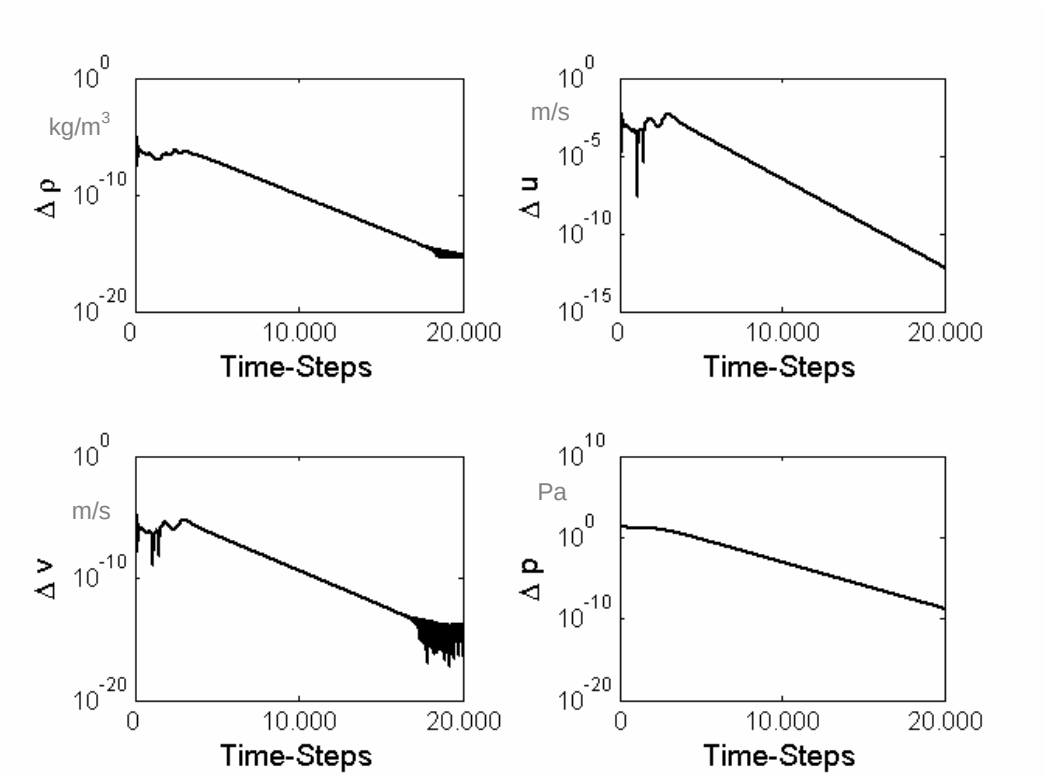


Figure 7.11 : Residuals (logarithmic) as a function of time-steps

## 7.3 The flank gap

The influence of the rotating flanks, which define the flank gap and also present two velocity boundary conditions as moving walls can be seen in figure 7.12 as a velocity vector plot. The reason for the high concentration of velocity vectors at both ends lies in high number of cells, which are becoming smaller and smaller.

Figure 7.13 shows, the velocity vector plot of the fluid, which flows between the rotating flanks and is also driven by a negative pressure gradient. The contour plot of the total velocity in the middle of the flank gap (y=0), is shown in figure 7.14. The positions of both velocity maximums are self-evident from the velocity boundary conditions of figure 7.12 or the fact that large distances from the centre of rotation will lead to high wall velocities. The positions correlate with the positions of a large radius of the rotating flanks and therefore high velocities.

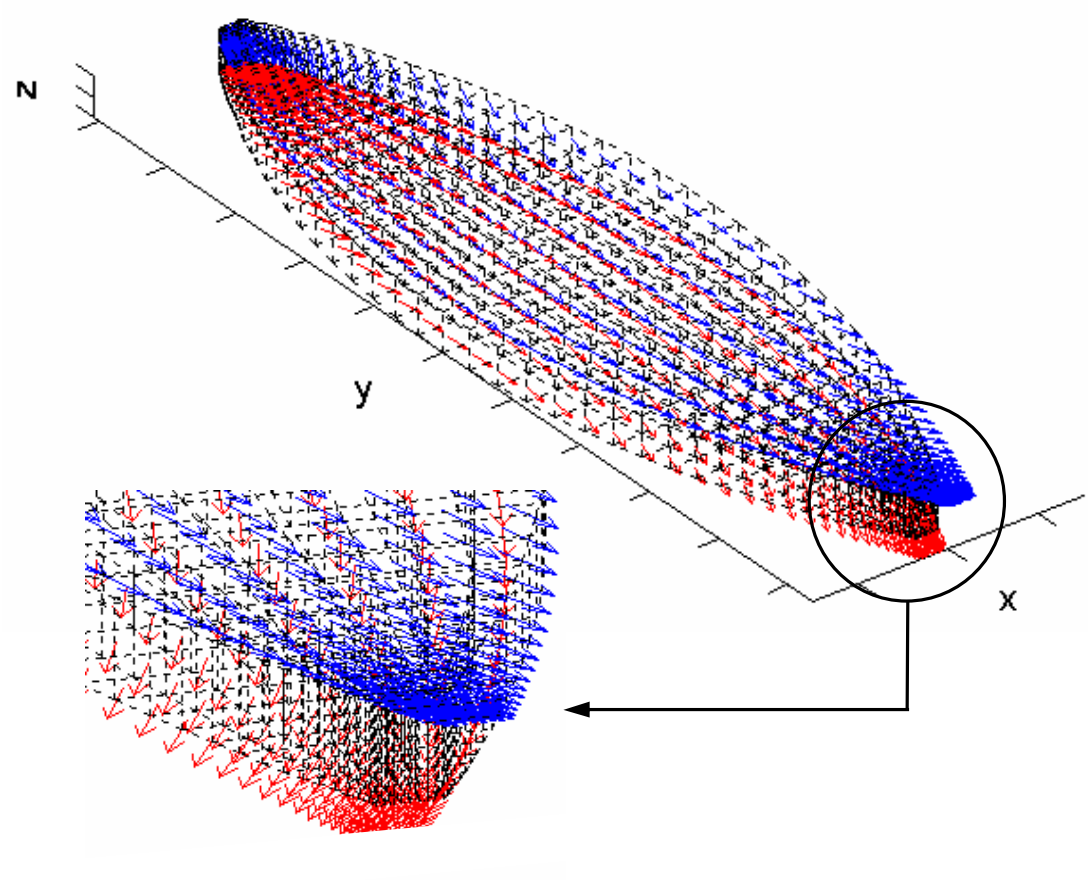


Figure 7.12 : Velocity boundary conditions

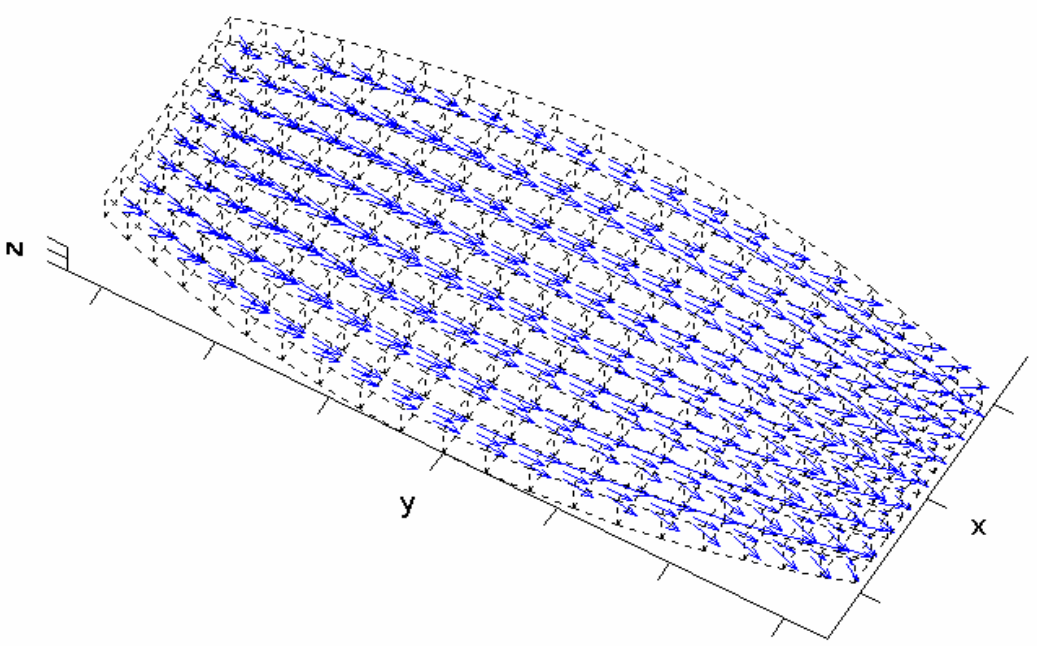


Figure 7.13 : Velocity vector plot (middle section)

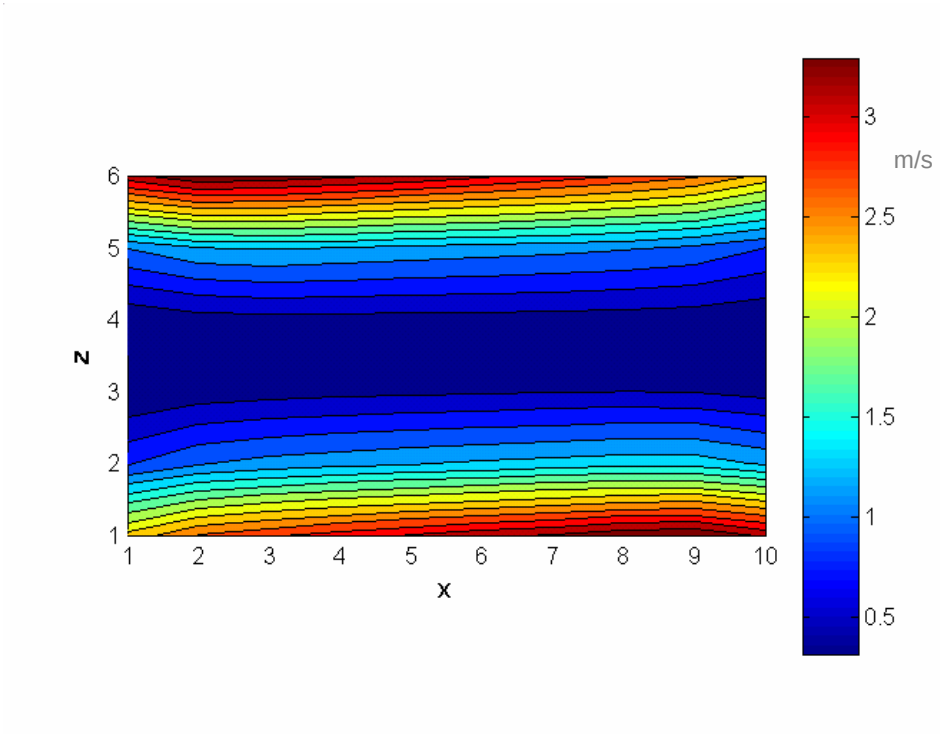


Figure 7.14 : Contour plot of the total velocity

## 8. Conclusion

The compressible flow through the perimeter gap, radial gap and the flank gap is responsible for the leakage of the whole screw pump. The exact calculation of the leakage flow rate and thus the net flow rate of the pump could be carried out by computational fluid dynamics. A finite volume model, which is programmed and solved in MATLAB, will be able to determine the one-, two- and three-dimensional distributions of the fluid variables density, velocities in all domain directions, pressure and temperature inside the gaps. The program has a very flexible structure and parametric studies concerning the boundary conditions are possible. The boundary conditions are easily defined by the density and velocities at the inlet, the pressure at the outlet, the moving walls and the geometry of the corresponding type of gap. Due to the compressibility of the fluid, which was taken into consideration with this finite volume model, the thermodynamic behaviour could be estimated. This fact will be particularly important in the field of multiphase operations with very high gas-volume-fractions, where the poor liquid phase is not able to absorb the compression heat of the gaseous phase.

## Nomenclature

**General Symbols**

| | |
|---|---|
| a | speed of sound |
| A | area of a cell face |
| c | specific heat capacity |
| e | specific internal energy |
| E | total internal energy |
| H | total enthalpy |
| k | thermal conductivity |
| p | static pressure |
| R | gas constant |
| t | time |
| T | temperature |
| u, v, w | velocity component in x, y and z - direction |
| **v** | total flow speed |
| V | cell volume |
| x, y, z | coordinates |

**Vectors / Matrices**

| | |
|---|---|
| **A** | normal vector multiplied by the cell face area ; Roe Matrix |
| **I** | parts of the Navier-Stokes equation, which are differentiated with respect to t |
| **J, K, L** | parts of the Navier-Stokes equation, which are differentiated with respect to x, y and z |
| **n** | normal vector |
| **P** | vector of primitive flow variables |
| **Q** | preconditioning matrix |

**Greek Letters**

| | |
|---|---|
| $\alpha$ | Runge-Kutta factor |
| $\mu$ | dynamic viscosity |
| $\rho$ | density |
| $\tau$ | shear stress |
| $\Theta$ | auxiliary term in the preconditioning matrix |

**Subscripts**

| | |
|---|---|
| c | convective |
| d | diffusive |
| E, N, S, W | cardinal points : east, north, south and west |
| i, j, k | cell indicators |

| | |
|---|---|
| l | cell face area index |
| L | lower ; left |
| m | coordinate direction index |
| p | constant pressure ; derivation with respect to pressure at constant temperature |
| R | right |
| T | derivation with respect to temperature at constant pressure |
| U | upper |
| v | constant volume |
| V | volume |
| x, y, z | coordinates |

**Superscripts**

| | |
|---|---|
| n | current time step |
| n+1 | following time step |

## References


[1] WINCEK, M.:
Zur Berechnung des Förderverhaltens von Schraubenspindelpumpen bei der Förderung von Flüssigkeits / Gas-Gemischen, Dissertation,
Universität Erlangen-Nürnberg, 1992
( The calculation of the conveyance behaviour of screw pumps at the conveyance of liquid/gas-mixtures, Ph.D. thesis, University of Erlangen-Nuremberg, 1992 )

[2] KÖRNER, H.:
Zum Förderverhalten von Schraubenspindelpumpen für Zweiphasengemische hohen Gasgehalts, Dissertation,
Universität Erlangen-Nürnberg, 1998
( The conveyance behaviour of screw pumps for two-phase mixtures with high gas-volume-fractions, Ph.D. thesis, University of Erlangen-Nuremberg, 1998 )

[3] ETZOLD, S.:
Verlustanalyse von Schraubenspindelpumpen bei Mehrphasenförderung,
Dissertation, Universität Hannover, 1993
( Leakage analysis of screw pumps during multiphase conveyance,
Ph.D. thesis, University of Hanover, 1993 )

[4] KILANI, M.I. / JAW, S.Y. / HAIK, Y. / CHEN, C.J.:
Numerical simulation of flow in a screw pump,
Fourteenth Engineering Mechanics Conference, EM 2000
American Society of Civil Engineers, May 21-24, 2000

[5] OERTEL JR., H. / LAURIEN, E.:
Numerische Strömungsmechanik ( Numerical fluid mechanics ), Springer-Verlag, Berlin Heidelberg, 1995

[6] WENDT, J.F.:
Computational Fluid Dynamics, Springer-Verlag,
Berlin Heidelberg, 1996

[7] BLAZEK, J.:
Computational Fluid Dynamics: Principles and Applications, Elsevier,
Oxford, 2001

[8] WEISS, J.M. / SMITH, W.A.:
Preconditioning applied to variable and constant density flows,
AIAA Journal, Volume 33, Number 11, Pages 2050-2057